

Lattice Mismatch-Driven In-Plane Strain Engineering for Enhanced Upper Critical Fields in Mo₂N Superconducting Thin Films

Aditya Singh¹, Divya Rawat¹, Victor Hjort², Abhisek Mishra³, Arnaud le Febvrier⁴, Subhankar Bedanta³, Per Eklund^{2,4}, and Ajay Soni^{1*}*

¹School of Physical Sciences, Indian Institute of Technology Mandi, Mandi 175005, Himachal Pradesh, India.

²Thin Film Physics Division, Department of Physics, Chemistry, and Biology (IFM), Linköping University, Linköping, SE-58183, Sweden.

³Laboratory for Nanomagnetism and Magnetic Materials (LNMM), School of Physical Sciences, National Institute of Science Education and Research (NISER), An OCC of Homi Bhabha National Institute (HBNI), Jatni 752050 Odisha, India.

⁴Department of Chemistry - Ångström Laboratory; Inorganic Chemistry, Uppsala University, Uppsala, 75105, Sweden

Emails: per.eklund@kemi.uu.se and ajay@iitmandi.ac.in

Transition metal nitrides are a fascinating class of hard coating material that provide an excellent platform for investigating superconductivity and fundamental electron-phonon (*e-ph*) interactions. In this work, the structural, morphological, and superconducting properties have been studied for Mo₂N thin films deposited via direct current magnetron sputtering on c-plane Al₂O₃ and MgO substrates to elucidate the effect of internal strain on superconducting properties. High-resolution X-Ray diffraction and time-of-flight-elastic recoil detection analysis confirms the growth of single-phase Mo₂N thin films exhibiting epitaxial growth with twin-domain structure. Low-temperature electrical transport measurements reveal superconducting transitions at ~ 5.2 K and ~ 5.6 K with corresponding upper critical fields of ~ 5 T and ~ 7 T for the films deposited on Al₂O₃ and MgO, respectively. These results indicate strong type-II superconductivity and the observed differences in superconducting properties are attributed to substrate-induced strain, which leads to higher *e-ph* coupling for the film on MgO substrate. These findings highlight the tunability of superconducting properties in Mo₂N films through strategic substrate selection.

Superconductivity in thin films has garnered significant attention due to their well-defined geometry, enhanced surface-to-volume ratio and remarkable sensitivity to external stimuli making them ideal candidates for a diverse technological applications including single-photon detectors, superconducting quantum interference devices and quantum computing. [1, 2] The ability to tune the superconductivity in epitaxial thin films, in comparison to the bulk counterparts, enables precise control over critical parameters such as carrier density, conformality to curved surfaces thus allowing functionalities like manipulation of magnetic flux and switching in Josephson junctions. [3] Among the various material systems explored

for thin film functionalities, the Transition Metal nitrides (TMNs) stand out due to their multidisciplinary array of technological applications arising from their thermal stability, refractory character and chemical resistance. [4-6] Epitaxial growth of thin film of TMNs on various substrates allows for precise control of morphology and structures at atomic-level, further enhancing their potential for advanced quantum technologies. TMNs display a range of functional properties, including superconductivity, [7, 8] quantum magnetism, [9, 10] exceptional hardness [11-13] making them suitable for applications in electronics, energy storage, photocatalysis, supercapacitor electrodes and beyond.[5, 13]

Within the TMN family, niobium, scandium and titanium nitrides have been widely studied for their superconducting behaviour, thermal managements and compatibility with device integration.[14-16] However, molybdenum nitrides (Mo–N) present a more complex case owing to their rich phase diagram, where even minor changes in temperature or nitrogen content can lead to multiple competing phases.[17] Previous research on Mo₂N_x systems have explored the impact of nitrogen and argon content in the plasma during the sputtering on the superconducting properties,[18] magnetization behaviour of different Mo₂N_x phases,[19] thickness-dependent superconducting properties of Mo₂N films grown on AlN-buffered Si substrates,[20] surface-induced suppressed superconductivity using low-temperature tunnelling spectroscopy.[21] Despite these efforts, comprehensive investigations on phase-pure Mo₂N thin films grown on substrates such as Al₂O₃ (MN/Al₂O₃) and MgO (111) (MN/MgO) is lacking, particularly where the detailed structural and low-temperature studies are involved. Moreover, recent theoretical predictions, [22] using Eliashberg formalism estimate a superconducting critical temperature (T_c) \sim 15.8 K for Mo₂N with a strong e - ph coupling constant of \sim 1.2. These findings highlight the need for experimental validation, particularly since strain induced by lattice mismatch can modify the e - ph interactions and potentially enhance superconducting properties. In general, the in-plane compressive strain flattens the electronic bands leading to enhanced density of state near fermi energy thereby elevating the superconducting T_c . [23]

In this work, we report a detailed study on superconductivity in phase-pure cubic Mo₂N thin films grown on c-plane Al₂O₃ and MgO (111) substrates, via DC reactive magnetron sputtering. The films exhibit a well-defined twin domain structure, as confirmed by X-ray diffraction (XRD) and pole figure analysis. Composition and stoichiometry are determined using Time-of-Flight Elastic Recoil Detection Analysis (ToF-ERDA), affirming near-ideal nitrogen incorporation. [the details are presented in supporting information Figure S1]

Temperature dependent electrical transport measurements reveal superconducting transitions with T_c up to ~ 5.5 K. The upper critical field (H_{c2}) for the MN/MgO shows a significant enhancement ($\sim 25\%$) from MN/Al₂O₃. Despite having same composition, the enhancement is related to the effect of in-plane compressive strain on the MN/MgO as compared to the in-plane tensile strain on the MN/Al₂O₃, which leads to the modulation of cooper pair formation. Magnetic measurements provide the details of lower critical fields (H_{c1}), coherence lengths, and penetration depths, which supports the robust type -II superconducting character of the films. Additionally, the Debye temperature of the thin films is estimated from fitting of thermal response of resistance with Bloch-Grüneisen model, and suggests a critical insight into $e-ph$ interactions. These results demonstrate that epitaxial MN/MgO can serve as a viable platform for superconducting applications with tunable physical properties.

Results and Discussion:

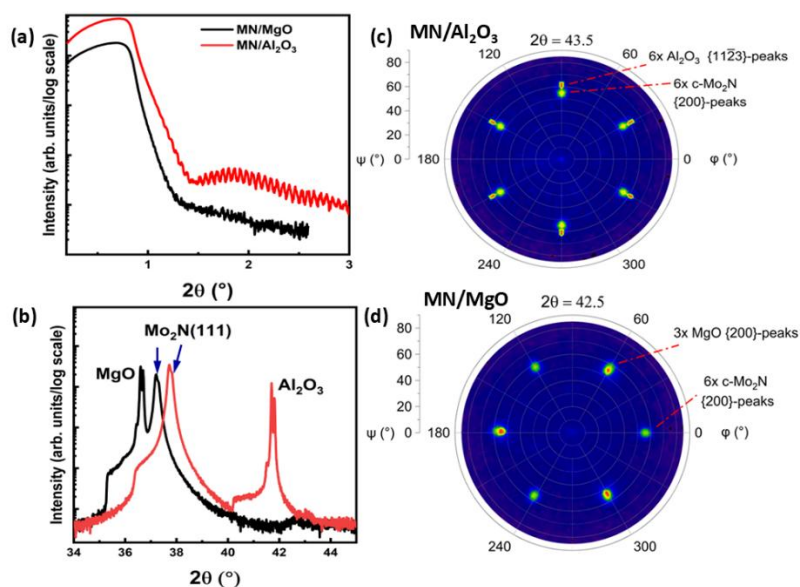


Figure 1 (a) XRR plot for MN/Al₂O₃ and MN/MgO (XRR is shifted vertically for visual clarity), (b) θ -2 θ XRD patterns. Pole figures indicating single phase epitaxial growth for (c) MN/Al₂O₃ and (d) MN/MgO.

The composition of the films is determined from the ERDA (Figure S1 and Table S1 in Supporting Information file), and found to be Mo₂N_{0.96} and Mo₂N_{0.97} for MN/Al₂O₃ and MN/MgO, respectively, which is very close to the stoichiometric Mo₂N phase, within the error limits. The thickness of the films is estimated by X-Ray Reflectivity (XRR) (Figure 1(a)) and are found to be $\sim 130 \pm 5$ nm with estimated roughness of ~ 2 nm and ~ 5 nm for MN/Al₂O₃ and MN/MgO, respectively. The mass density of the films extracted from XRR are presented in table S1 in Supporting Information. Figure 1(b) displays the XRD patterns of the two samples, where the substrate peaks for (0001) Al₂O₃ and (111) MgO are visible at $2\theta \sim 41.7^\circ$ (PDF 00-046-1212) and at $2\theta \sim 36.6^\circ$ (PDF 01-071-6452), respectively. The peak at $2\theta \sim 37.7^\circ$ (d-spacing 2.38 Å) for MN/Al₂O₃ and $2\theta \sim 37.2^\circ$ (d-spacing 2.42 Å) for MN/MgO corresponds to the (111) plane of cubic Mo₂N with a dominant out-of-plane orientation. The shift in the intense MN-111 peak is because of the substrate driven stress. The in-plane orientation of the films is further demonstrated by the pole figure analysis of the 200-reflection of Mo₂N, observed at $2\theta \sim 43.5^\circ$ for MN/Al₂O₃ and $\sim 42.5^\circ$ for MN/MgO, as shown in Figure 1(c-d). The six poles of Al₂O₃ 11 $\bar{2}$ 3, at $\Psi = 61.5^\circ$ and six poles of c-Mo₂N 200, at $\Psi = 55.5^\circ$ in Figure 1(c) indicates epitaxial twin-domain growth, a common feature for cubic structures on both the substrates.[24-26] In Figure 1 (d) three prominent poles are observed at $\Psi = 54.7^\circ$,

corresponding to MgO 200-reflections from the substrate alongside six poles from the Mo₂N (200) planes, spaced every 60° in ϕ , with some overlapping the MgO poles. Since both MgO and Mo₂N are cubic, their 200 poles are expected to align at $\Psi = 54.7^\circ$ in a stress-free state. However, the Mo₂N poles appear at a slightly higher Ψ ($\sim 55.5^\circ$), indicating in-plane compressive strain in the film consistent with observations in Figure 1(b). The epitaxial relationship of Mo₂N on both substrates is as follows: $(111)_{\text{Mo}_2\text{N}} \parallel (0001)_{\text{Al}_2\text{O}_3}$ (out-of-plane) and $[11\bar{2}]_{\text{Mo}_2\text{N}} \parallel [10\bar{1}0]_{\text{Al}_2\text{O}_3}$ (in-plane); and $(111)_{\text{Mo}_2\text{N}} \parallel (111)_{\text{MgO}}$ (out-of-plane) and $[110]_{\text{Mo}_2\text{N}} \parallel [110]_{\text{MgO}}$. The morphological studies as well as the AFM images reveal a smooth surface with voids and grain boundaries, provided in the Supporting Information file (Figure S2 (a-d)).

Comprehensive characterization using ERDA, XRD and pole figure confirms that both films consist of a single-phase Mo₂N with identical composition. Epitaxial growth is observed on both c-plane Al₂O₃ and MgO (111) substrates, with twin domains present in each case. Despite the consistent composition, a notable shift in the XRD peak positions is observed between the two films, attributed to strain induced by their epitaxial relationship with the respective substrates. Comparing with the XRD peaks of stress-free Mo₂N (37.4°) as a reference, the MN/Al₂O₃ film exhibits a peak shift indicative of in-plane tensile strain, while the MN/MgO film shows a shift consistent with in-plane compressive strain.

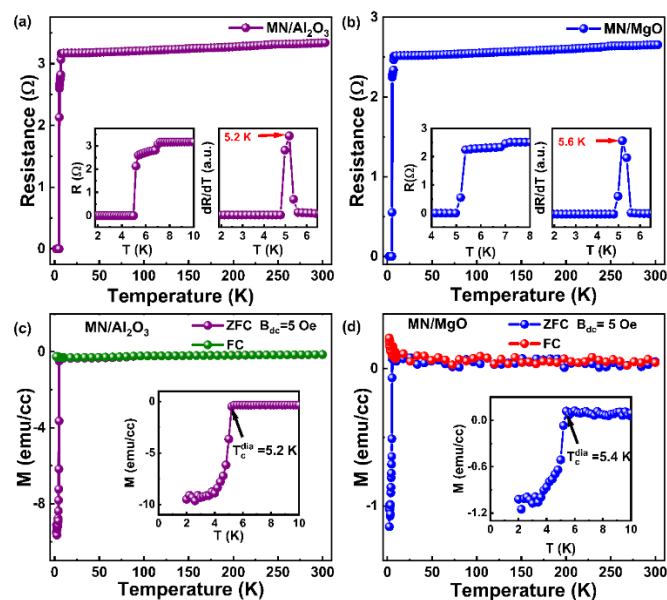


Figure 2. Temperature dependent resistance of (a) MN/Al₂O₃ and (b) MN/MgO. The inset shows dR/dT plots for estimation of T_c , and temperature dependent magnetization of (c) MN/Al₂O₃ and (d) MN/MgO. The T_c in insets is supporting the observation in transport measurements with in the error limits of the techniques.

The onset of superconductivity in the thin films is estimated from electrical transport and magnetization measurements. The R (300 K) for the films is $\sim 3.33 \Omega$ and $\sim 2.65 \Omega$ for MN/Al₂O₃ and MN/MgO, respectively, which is attributed to the increased grain boundary scattering in the MN/Al₂O₃ as compared to MN/MgO (Figure S2(c-d)). In order to study the quality of thin films, the residual resistivity ratio, $RRR = \frac{\rho(300\text{ K})}{\rho(6\text{ K})}$, is calculated for both the thin films which is found to be ~ 1.22 for MN/Al₂O₃ and 1.14 for MN/MgO. The significantly higher RRR compared to previously reported Mo₂N thin films on Si substrates ($RRR \sim 0.9$) [20], indicates a superior crystallinity, reduced defect density, and larger grain sizes with fewer macroscopic imperfections. The R - T data (Figure 2 (a-b)) confirms the metallic nature of the films with the T_c estimated from the derivative plot of resistance (inset of Figure 2 (a-b)), which shows the $T_c \sim 5.2$ K (for MN/Al₂O₃) and $T_c \sim 5.6$ K (for MN/MgO). The estimated T_c is further corroborated by magnetization measurements of the Meissner effect (Figure 2(c-d)). Magnetization data (M - T) obtained using both field-cooled (FC) and zero-field-cooled (ZFC) protocols exhibit robust diamagnetic behaviour with a $T_c^{dia} = 5.2$ K and $T_c^{dia} = 5.4$ K, for MN/Al₂O₃ and MN/MgO, respectively. Furthermore, the M - T data in both ZFC and FC protocols are separated thus confirming the presence of flux pinning in the films.[27, 28] In order to rule out the possibility of substrate induced superconductivity, M - T measurements of bare substrates (Figure S3 (a-b)) are performed, showing no signs of superconductivity. The higher T_c for the MN/MgO film as compared to MN/Al₂O₃ is associated with the compressive in-plane strain. [29] Two-step superconducting transitions, (inset of Figure 2 (a-b)), commonly arise from applied forces such as pressure, magnetic fields, strain, proximity effects and is observed in several other thin films as well. [30-32] The temperature dependence of resistivity above the T_c (9 K-200 K) is analysed using the Bloch Grüneissen (BG) model, [33] by taking account of the e - ph interactions. The fitting of the resistivity data (Figure S4) strongly suggests that e - ph interactions are the dominant scattering mechanism for Mo₂N thin films.[34] The e - ph coupling strength, estimated using McMillan's relation[35] with a Coulomb pseudopotential $\mu^* = 0.13$, is found to be ~ 0.75 for MN/Al₂O₃ and ~ 0.76 for MN/MgO (Section D in Supporting Information). This result highlights the enhancement of e - ph interactions due to compressive strain in MN/MgO compared to the tensile strain in MN/Al₂O₃.

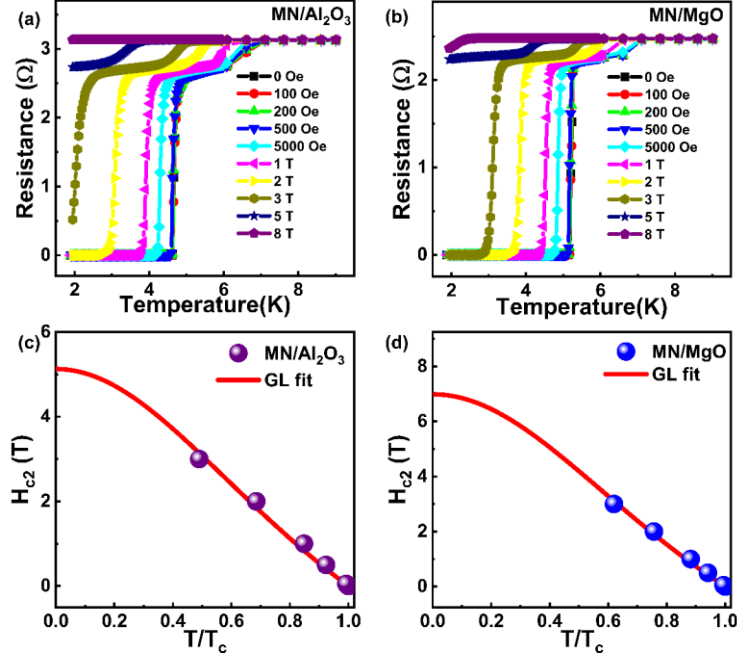


Figure 3: Low temperature magnetoresistance measurements for (a) MN/Al₂O₃ and (b) MN/MgO. Upper critical field with Ginzburg-Landau fitting of (c) MN/Al₂O₃ and (d) MN/MgO.

Low-temperature magnetoresistance measurements (Figure 3 (a-b)) revealed an increasing T_c width with applied magnetic field, which is a characteristic signature of type-II superconductors.[36] The upper critical field H_{c2} , is estimated using the T_c^{onset} criterion, with the normal state resistance taken at ~ 6.1 K and by fitting the data with the Ginzburg-Landau (GL) model with an extrapolation to determine the $H_{c2}(0)$ for both films. According to the GL model, the critical field at a temperature, T is given by $H_{c2}(T) = H_{c2}(0) \frac{(1-t^2)}{(1+t^2)}$, where t is the reduced temperature given by $t = \frac{T}{T_c}$ and $H_{c2}(0)$ is critical field at 0 K. Based on this model, the estimated $H_{c2}(0)$ is found to be ~ 5.1 T for MN/Al₂O₃ and ~ 7 T for MN/MgO, which is more than 25% enhancement in the MN/MgO then MN/Al₂O₃.

The enhancements is attributed to the increased flux pinning potential resulting from a compressive in-plane strain on MN/MgO in contrasts with the tensile in-plane strain in MN/Al₂O₃ and also correlates with enhanced the $e-ph$ interactions.[23, 37, 38] To understand further on the nature of the superconductivity and the limiting mechanism of the copper pair formation, it is important to dive deeper into the mechanism governing H_{c2} . For this, the Werthamer-Helfand-Hohenberg (WHH) formula $H_{c2}^{orb}(0) = -0.693T_c \left(\frac{dH_{c2}}{dT} \right)_{T=T_c}$, [39] is

used for estimation of the zero-temperature orbital limited upper critical field, $H_{c2}^{orb}(0)$. The calculated values are ~ 4.4 T for MN/Al₂O₃ and ~ 5.8 T for MN/MgO. These estimates are lower than the H_{c2} estimated from GL fitting. In general, the upper limit on H_{c2} is given by the Pauli Paramagnetic limit, which is given by $H_p = 1.86T_c$ (9.6 T for MN/Al₂O₃ and 10.3 T for MN/MgO). The estimation and analysis clearly indicates a conventional BCS type superconductivity.[40]. To understand the mechanisms of Cooper pair breaking in type-II superconductors under an applied magnetic field, both orbital and spin-paramagnetic effects on the H_{c2} are considered. According to the Maki theory, the Maki parameter (α), which quantifies the relative strength of these effects, is defined as $\alpha = \sqrt{2} \frac{H_{c2}^{orb}(0)}{H_p(0)}$, [41]. The α values are found to be ~ 0.64 (for MN/Al₂O₃) and ~ 0.8 (MN/MgO), both less than 1, confirming that the superconductivity in Mo₂N thin films is limited by orbital depairing mechanisms. The GL coherence length (ξ_{GL}), is calculated by $\xi_{GL} = \sqrt{\frac{\phi_0}{2\pi H_{c2}(0)}}$, where $\phi_0 = 2.068 \times 10^{-15}$ T.m² is magnetic flux quantum. The coherence length is found out to be ~ 8.01 nm and ~ 6.85 nm for MN/Al₂O₃ and MN/MgO films, respectively.

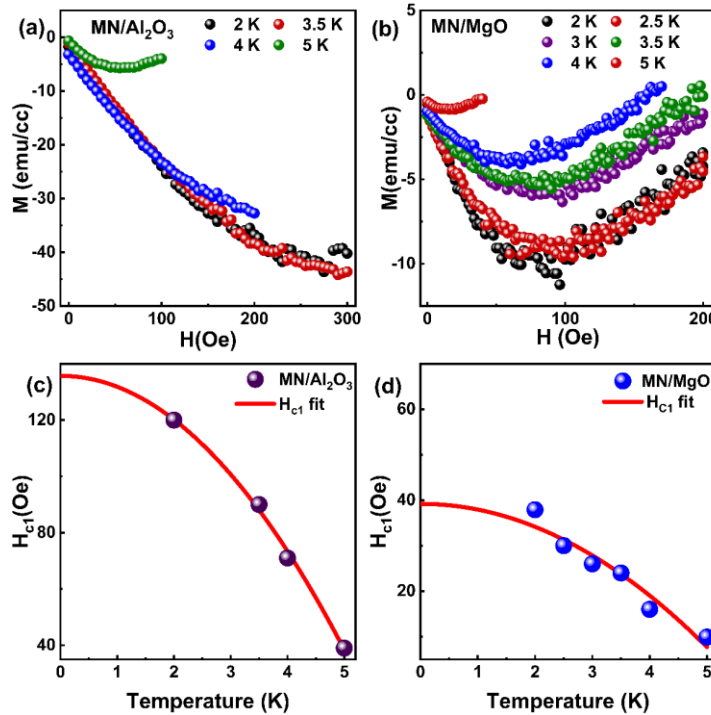


Figure 4: M - H plots (a-b) and H_{c1} vs T (c-d) plots of MN/Al₂O₃ and MN/MgO respectively.

Table 1: Superconducting parameters of MN/Al₂O₃ and MN/MgO.

Sample	Thickness (nm)	T_c (K)	H_{c1} (Oe)	$H_{c2}(0)$ (T)	$H_{c2}^{orb}(0)$ (T)	H_c (Oe)	ξ_{GL} (nm)	λ (nm)	α
MN/Al ₂ O ₃	130 – 135	5.18	135	5.12	4.37	1469	8.01	197	0.64
MN/MgO	130 – 135	5.57	39	6.98	5.83	814	6.85	416	0.8

In order to estimate the H_{c1} of the samples we have used the Meissner–Ochsenfeld criterion on the M - H measurements below T_c (Figure 4 a-b).[42] The obtained H_{c1} at different temperatures is analysed using the equation $H_{c1} = H_{c1}(0)[1 - \left(\frac{T}{T_c}\right)^2]$, where $H_{c1}(0)$ is lower critical field at 0 K. The obtained $H_{c1}(0)$ values for MN/Al₂O₃ and MN/MgO are found to be ~ 135 Oe and ~ 39 Oe, respectively. Further we have estimated the superconducting penetration depth (λ_{GL}) by $H_{c1} = \frac{\phi_0}{4\pi\lambda_{GL}^2} \ln\left(\frac{\lambda_{GL}}{\xi_{GL}}\right)$, and λ_{GL} is found to be ~ 197 nm and ~ 416 nm for MN/Al₂O₃ and MN/MgO respectively. The GL parameter (κ_{GL}) given by $\kappa_{GL} = \frac{\lambda_{GL}}{\xi_{GL}}$ is found to be ~ 24.6 and ~ 60.7 for MN/Al₂O₃ and MN/MgO, respectively. The values are much greater than $\frac{1}{\sqrt{2}}$, indicating a strong type-II superconductivity. To assess the superconducting condensation energy, the thermodynamical critical field (H_c), is evaluated using the relation $H_{c1}(0)H_{c2}(0) = H_c^2 \ln \kappa_{GL}$ and found to be ~ 1469 Oe for MN/Al₂O₃ and ~ 814 Oe for MN/MgO. All the characteristic superconducting parameters for both thin films are tabulated in Table 1.

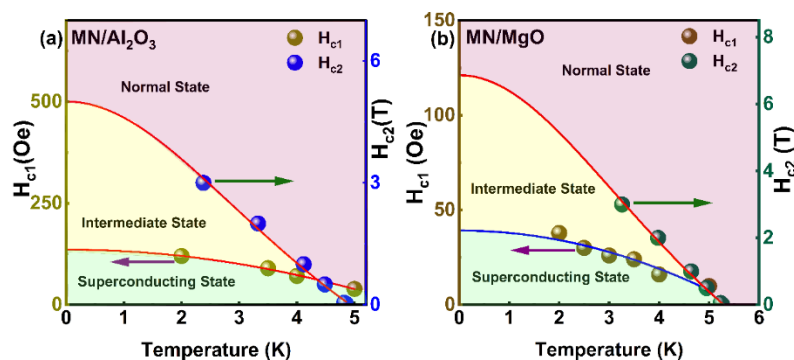


Figure 5. Phase diagram showing the superconducting, intermediate, and normal state of the (a) MN/Al₂O₃, (b)MN/MgO.

Considering both $H_{c1}(T)$ and $H_{c2}(T)$ for the films, the superconducting phase diagram is presented in Figures 5(a-b), showing distinct superconducting, intermediate, and normal

states. The detailed analysis of the phase diagram confirms the thin films to be a strong type-II superconductors. These findings highlight the potential of Mo₂N thin films for integration into next-generation superconducting quantum and power electronic devices.

Conclusion:

In summary a significant enhancement of $\sim 25\%$ in the H_{c2} of MN/MgO is attributed to *e-ph* modulation arising from compressive in-plane strain, which enhances flux-pinning potential and overall superconducting performance compared to the tensile-strained MN/Al₂O₃. These findings demonstrate the crucial role and impact of strain engineering in tuning the superconducting behavior of transition metal nitride thin films. This work paved the way for their application in kinetic inductance devices, superconducting qubits and miniaturization of superconducting interconnects for next-generation electronic technologies, highlighting the significant impact of strain on the superconducting properties of Mo₂N films.

Experimental Details:

Thin film deposition: Molybdenum nitride thin films were grown, on sapphire (Al₂O₃ (0001)) and MgO (111) substrates, by DC reactive magnetron sputtering in an ultrahigh vacuum chamber.[43] Before deposition, the MgO substrates were cleaned by multiple sonication cycles first in (i) a Hellmanex soap solution (~ 3 mins), followed by (ii) deionized water (two times for ~ 5 mins), (iii) acetone (~ 10 mins), (iv) ethanol (~ 10 mins) and finally dried with compressed nitrogen gas.[44] This procedure helps in the removal of possible hydroxides and the carbonates present on the surface. The substrates were kept in the deposition chamber and evacuated to a pressure of $\sim 8.9 \times 10^{-9}$ Torr and the substrate temperature was kept at $\sim 500^\circ$ C. The deposition of Mo₂N was carried out with a mixture of Argon and Nitrogen (flow rates of Ar ~ 22 sccm and N₂ ~ 33 sccm).

Characterisation Studies: The compositions of the films were determined by ToF-ERDA using ~ 36 MeV ¹²⁷I⁹⁺ ions as probing beam with a incidence angle $\sim 67.5^\circ$, and a recoil angle $\sim 45^\circ$. [45] The data were analysed using the Potku code.[46] The crystal structure was investigated by XRD using a PANalytical X'Pert Pro diffractometer in Bragg-Brentano geometry and equipped with a Cu K α source operated at ~ 45 kV and ~ 40 mA. The incident optics had a $\sim 0.5^\circ$ divergence slit and a 0.5° anti-scatter slit, and the diffracted optics included a ~ 5.0 mm anti-scatter slit, a 0.04 rad Soller slit, a Ni-filter, an X'Celerator detector measuring in $\sim 0.008^\circ$ steps sizes with an equivalent counting time of ~ 19 s per step. For XRR, the PANalytical X'Pert Pro diffractometer was operated in line-mode with a hybrid mirror module with $\sim 0.5^\circ$ divergence slit for incident optics and a $\sim 0.125^\circ$ divergence slit for the diffracted optics. For pole figure, the instrument was operated in point-mode with crossed-slit module set

at 2 x 2 mm as incident optics, and a $\sim 0.27^\circ$ parallel plate collimator for diffracted optics. Scanning electron microscopy (SEM) was performed using a Zeiss Sigma 300 with the field emission gun was operated at 2 kV. The atomic force microscopy (AFM) images of the films were taken using Bruker Dimension icon AFM.

Physical and Magnetic properties measurements: The low temperature electrical transport properties were performed using the physical property measurement system (PPMS, Quantum Design make). The temperature dependent magnetization measurements were carried out using an MPMS3 SQUID-VSM magnetometer (Quantum Design make). In the zero-field-cooled (ZFC) protocol, the sample was first cooled from room temperature down to ~ 2 K in the absence of external magnetic field and the magnetization was recorded during the subsequent warming cycle in the presence of a ~ 50 e field. For the FC measurement, the sample was cooled in the presence of the same constant external magnetic field and the magnetization was recorded continuously during this cooling process.

Acknowledgement: AS acknowledge IIT Mandi for research facilities and DST India for Indo-Sweden bilateral grant (Grant No. DST/INT/SWD/VR/P-18/2019). PE acknowledges funding from the Swedish Government Strategic Research Area in Materials Science on Functional Materials at Linköping University (Faculty Grant SFO-Mat-LiU No. 2009 00971), the Knut and Alice Wallenberg foundation through the Wallenberg Academy Fellows program (KAW-2020.0196, P.E.), and the Swedish Research Council (VR) under Project No. 2021-03826. AM and SB thank the Department of Atomic Energy (DAE), Government of India for the financial support.

Data Availability

The data that support the findings of this study are available from the corresponding author upon reasonable request.

References:

1. A. Engel, A. Aeschbacher, K. Inderbitzin, A. Schilling, K. Il'in, M. Hofherr, M. Siegel, A. Semenov, and H.-W. Hübers, *Tantalum nitride superconducting single-photon detectors with low cut-off energy*. Applied Physics Letters, 2012. **100**(6).
2. J. del Valle, J. G. Ramírez, M. J. Rozenberg, and I. K. Schuller, *Challenges in materials and devices for resistive-switching-based neuromorphic computing*. Journal of Applied Physics, 2018. **124**(21).
3. Y. Zou, Q. Jin, Y. Wang, K. Jiang, S. Wang, Y. Li, E.-J. Guo, and Z. G. Cheng, *Tuning superconductivity in vanadium nitride films by adjusting strain*. Physical Review B, 2022. **105**(22): p. 224516.
4. Y. Zhou, W. Guo, and T. Li, *A review on transition metal nitrides as electrode materials for supercapacitors*. Ceramics International, 2019. **45**(17): p. 21062-21076.

5. S. A. Rasaki, B. Zhang, K. Anbalgam, T. Thomas, and M. Yang, *Synthesis and application of nano-structured metal nitrides and carbides: A review*. Progress in Solid State Chemistry, 2018. **50**: p. 1-15.
6. R. Ningthoujam and N. Gajbhiye, *Synthesis, electron transport properties of transition metal nitrides and applications*. Progress in Materials Science, 2015. **70**: p. 50-154.
7. E. Isaev, R. Ahuja, S. Simak, A. Lichtenstein, Y. K. Vekilov, B. Johansson, and I. Abrikosov, *Anomalously enhanced superconductivity and ab initio lattice dynamics in transition metal carbides and nitrides*. Physical Review B, 2005. **72**(6): p. 064515.
8. S. Wang, D. Antonio, X. Yu, J. Zhang, A. L. Cornelius, D. He, and Y. Zhao, *The hardest superconducting metal nitride*. Scientific reports, 2015. **5**(1): p. 13733.
9. L. M. Corliss, N. Elliott, and J. M. Hastings, *Antiferromagnetic Structure of CrN*. Physical Review, 1960. **117**(4): p. 929-935.
10. Q. Jin, et al., *Strain-Mediated High Conductivity in Ultrathin Antiferromagnetic Metallic Nitrides*. Advanced Materials, 2021. **33**(2): p. 2005920.
11. X.-J. Chen, et al., *Hard superconducting nitrides*. Proceedings of the National Academy of Sciences, 2005. **102**(9): p. 3198-3201.
12. S. T. Oyama, *Introduction to the chemistry of transition metal carbides and nitrides*, in *The Chemistry of Transition Metal Carbides and Nitrides*, S.T. Oyama, Editor. 1996, Springer Netherlands: Dordrecht. p. 1-27.
13. Y. Zhong, X. Xia, F. Shi, J. Zhan, J. Tu, and H. J. Fan, *Transition Metal Carbides and Nitrides in Energy Storage and Conversion*. Advanced Science, 2016. **3**(5): p. 1500286.
14. N. Kokubo and B. Gerelkhuu, *NbTiN SQUID-on-tip fabricated by self-aligned deposition using reactive DC magnetron sputtering*. Applied Physics Letters, 2024. **124**(26).
15. D. Zhang, et al., *The on-chip scanning probe with dual niobium nitride nanoscale superconducting quantum interference devices for magnetic imaging at the high temperature*. Superconductor Science and Technology, 2023. **36**(12): p. 125003.
16. N. Tureson, et al., *Effect of ion-implantation-induced defects and Mg dopants on the thermoelectric properties of ScN*. Physical Review B, 2018. **98**(20): p. 205307.
17. L. Stöber, J. P. Konrath, V. Haberl, F. Patocka, M. Schneider, and U. Schmid, *Nitrogen incorporation in sputter deposited molybdenum nitride thin films*. Journal of Vacuum Science & Technology A, 2016. **34**(2): p. 021513.
18. N. Haberkorn, S. Bengio, S. Suárez, P. D. Pérez, M. Sirena, and J. Guimpel, *Effect of the nitrogen-argon gas mixtures on the superconductivity properties of reactively sputtered molybdenum nitride thin films*. Materials Letters, 2018. **215**: p. 15-18.
19. K. Inumaru, K. Baba, and S. Yamanaka, *Superconducting molybdenum nitride epitaxial thin films deposited on MgO and α -Al₂O₃ substrates by molecular beam epitaxy*. Applied Surface Science, 2006. **253**(5): p. 2863-2869.
20. N. Haberkorn, S. Bengio, H. Troiani, S. Suárez, P. D. Pérez, P. Granell, F. Golmar, M. Sirena, and J. Guimpel, *Thickness dependence of the superconducting properties of γ -Mo₂N thin films on Si (001) grown by DC sputtering at room temperature*. Materials Chemistry and Physics, 2018. **204**: p. 48-57.
21. M. Kuzmiak, M. Kopčík, F. Košuth, V. Vaňo, P. Szabó, V. Latyshev, V. Komanický, and P. Samuely, *Suppressed Superconductivity in Ultrathin Mo₂N Films due to Pair-Breaking at the Interface*. Journal of Superconductivity and Novel Magnetism, 2022. **35**(7): p. 1775-1780.
22. J. Bekaert, C. Sevik, and M. V. Milošević, *First-principles exploration of superconductivity in MXenes*. Nanoscale, 2020. **12**(33): p. 17354-17361.
23. M. Abrecht, D. Ariosa, D. Cloetta, S. Mitrovic, M. Onellion, X. X. Xi, G. Margaritondo, and D. Pavuna, *Strain and High Temperature Superconductivity: Unexpected Results from Direct Electronic Structure Measurements in Thin Films*. Physical Review Letters, 2003. **91**(5): p. 057002.
24. P. Stampe, M. Bullock, W. Tucker, and R. J. Kennedy, *Growth of MgO thin films on M-, A-, C- and R-plane sapphire by laser ablation*. Journal of Physics D: Applied Physics, 1999. **32**(15): p. 1778.
25. R. Li, J. S. Gandhi, R. Pillai, R. Forrest, D. Starikov, and A. Bensaoula, *Epitaxial growth of (111)-oriented Zr_xTi_{1-x}N thin films on c-plane Al₂O₃ substrates*. Journal of crystal growth, 2014. **404**: p. 1-8.
26. Z. Dai, A. Miyashita, S. Yamamoto, K. Narumi, and H. Naramoto, *Crystalline and nearly stoichiometric vanadium nitride thin film by PLD*. Thin Solid Films, 1999. **347**(1-2): p. 117-120.

27. X. Bai, et al., *Charge-carrier-type controlled superconducting dome in ZrN_xO_y* . Physical Review Materials, 2023. **7**(9): p. 094801.
28. R. Jha, B. Tiwari, P. Rani, H. Kishan, and V. P. S. Awana, *Robust superconductivity with large upper critical field in Nb_2PdS_5* . Journal of Applied Physics, 2014. **115**(21).
29. F. Nabeshima, Y. Imai, M. Hanawa, I. Tsukada, and A. Maeda, *Enhancement of the superconducting transition temperature in $FeSe$ epitaxial thin films by anisotropic compression*. Applied Physics Letters, 2013. **103**(17): p. 172602.
30. B. Wang, K. Matsubayashi, Y. Uwatoko, and K. Ohgushi, *High Pressure Effect on the Superconductivity in VN* . Journal of the Physical Society of Japan, 2015. **84**(10): p. 104706.
31. I. Pentin, Y. Vakhtomin, V. Seleznev, and K. Smirnov, *Hot electron energy relaxation time in vanadium nitride superconducting film structures under THz and IR radiation*. Scientific Reports, 2020. **10**(1): p. 16819.
32. A. K. Verma, R. Gupta, S. Prakash, A. Gloskovskii, S. Kalal, P. Tiwari, V. R. Reddy, R. Rawat, and M. Gupta, *Structure and Superconductivity of Epitaxial and Polycrystalline VN Thin Films*. ACS Applied Electronic Materials, 2024. **6**(7): p. 5029-5035.
33. J. M. Ziman, *Electrons and phonons: the theory of transport phenomena in solids*. 2001: Oxford university press.
34. A. Bid, A. Bora, and A. K. Raychaudhuri, *Temperature dependence of the resistance of metallic nanowires of diameter $\geq 15nm$: Applicability of Bloch-Grüneisen theorem*. Physical Review B, 2006. **74**(3): p. 035426.
35. W. L. McMillan, *Transition Temperature of Strong-Coupled Superconductors*. Physical Review, 1968. **167**(2): p. 331-344.
36. A. S. Ilin, et al., *Superconductivity in thin films of RuN* . Physical Review Materials, 2024. **8**(7): p. 074801.
37. T. Horide, T. Maekawa, T. Aikawa, T. Kitamura, and K. Nakamura, *T_c and resistivity variation induced by external bending strain in flexible film of strain-sensitive $(La,Sr)_2CuO_4$* . Physical Review Materials, 2024. **8**(9): p. 094802.
38. R. Zhang, et al., *Wafer-Scale Epitaxy of Flexible Nitride Films with Superior Plasmonic and Superconducting Performance*. ACS Applied Materials & Interfaces, 2021. **13**(50): p. 60182-60191.
39. N. R. Werthamer, E. Helfand, and P. C. Hohenberg, *Temperature and Purity Dependence of the Superconducting Critical Field, H_{c2} . III. Electron Spin and Spin-Orbit Effects*. Physical Review, 1966. **147**(1): p. 295-302.
40. A. M. Clogston, *Upper Limit for the Critical Field in Hard Superconductors*. Physical Review Letters, 1962. **9**(6): p. 266-267.
41. K. Maki, *Effect of Pauli Paramagnetism on Magnetic Properties of High-Field Superconductors*. Physical Review, 1966. **148**(1): p. 362-369.
42. M. Falkowski, Z. Śniadecki, T. J. Bednarchuk, and A. Kowalczyk, *Structural and physical properties of the II-type superconductor Nb_5Si_2B* . Journal of Applied Physics, 2023. **133**(24).
43. A. Le Febvrier, L. Landälv, T. Liersch, D. Sandmark, P. Sandström, and P. Eklund, *An upgraded ultra-high vacuum magnetron-sputtering system for high-versatility and software-controlled deposition*. Vacuum, 2021. **187**: p. 110137.
44. A. Le Febvrier, J. Jensen, and P. Eklund, *Wet-cleaning of $MgO(001)$: Modification of surface chemistry and effects on thin film growth investigated by x-ray photoelectron spectroscopy and time-of-flight secondary ion mass spectroscopy*. Journal of Vacuum Science & Technology A, 2017. **35**(2).
45. M. Mayer, et al., *Ion beam analysis of fusion plasma-facing materials and components: facilities and research challenges*. Nuclear Fusion, 2019. **60**(2): p. 025001.
46. K. Arstila, et al., *Potku–New analysis software for heavy ion elastic recoil detection analysis*. Nuclear Instruments and Methods in Physics Research Section B: Beam Interactions with Materials and Atoms, 2014. **331**: p. 34-41.

Supporting Information

Lattice Mismatch-Driven In-Plane Strain Engineering for Enhanced Upper Critical Fields in Mo₂N Superconducting Thin Films

Aditya Singh¹, Divya Rawat¹, Victor Hjort², Abhisek Mishra³, Arnaud le Febvrier⁴, Subhankar Bedanta³, Per Eklund^{2,4,*}, and Ajay Soni^{1,*}

¹School of Physical Sciences, Indian Institute of Technology Mandi, Mandi 175005, Himachal Pradesh, India.

²Thin Film Physics Division, Department of Physics, Chemistry, and Biology (IFM), Linköping University, Linköping, SE-58183, Sweden.

³Laboratory for Nanomagnetism and Magnetic Materials (LNMM), School of Physical Sciences, National Institute of Science Education and Research (NISER), An OCC of Homi Bhabha National Institute (HBNI), Jatni 752050 Odisha, India.

⁴Department of Chemistry - Ångström Laboratory; Inorganic Chemistry, Uppsala University, Uppsala, 75105, Sweden

Emails: per.eklund@kemi.uu.se and ajay@iitmandi.ac.in

The supporting information has the additional details of characterization and experiments complementing to the main text.

(A) Time-of-Flight Elastic Recoil Detection Analysis (ToF-ERDA):

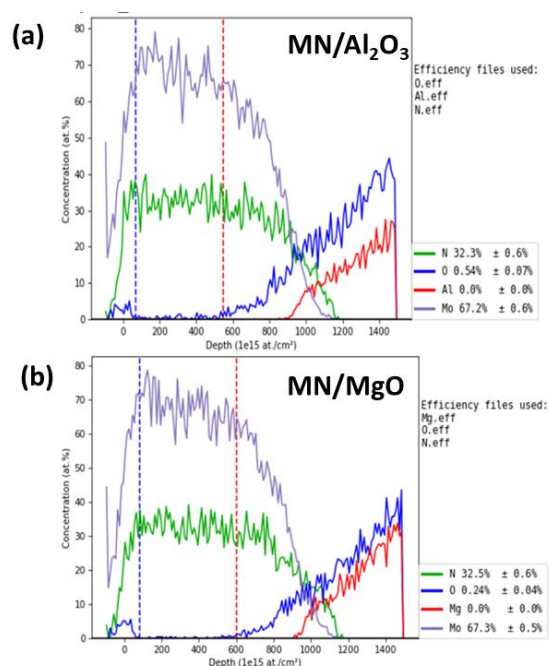


Figure S1: ToF-ERDA of (a) MN/Al₂O₃ and (b) MN/MgO.

The ERDA depth profiles (Figure S1. (a-b)) for MN/Al₂O₃ and MN/MgO show uniform elemental distributions of N and Mo across the measured depth range. No significant contribution of Al or Mg is detected in the measured depth range, which can be expected to be coming from the substrates. In the fitting model for XRR, a very thin layer of 3.4 ± 1 nm of oxide is used for the convergence of fitting parameter and is considered to be present on both films due to post-oxidation, once the sample is out of the deposition chamber. The elemental composition of the films along with the density and roughness as extracted from the ERDA and XRR measurements are detailed in Table S1.

Table S1. Elemental composition, density, and roughness of the films.

Films/Substrate	Composition from ERDA, (± 3%)		Density and Roughness from XRR	
	Mo ₂ N _x	O-contamination	Density [g cm ⁻³]	Roughness (nm)
MN/Al ₂ O ₃	Mo ₂ N _{0.96}	0.6 %	8.9 ± 0.1	2 ± 1
MN/MgO	Mo ₂ N _{0.97}	0.2 %	8.8 ± 0.1	5 ± 2

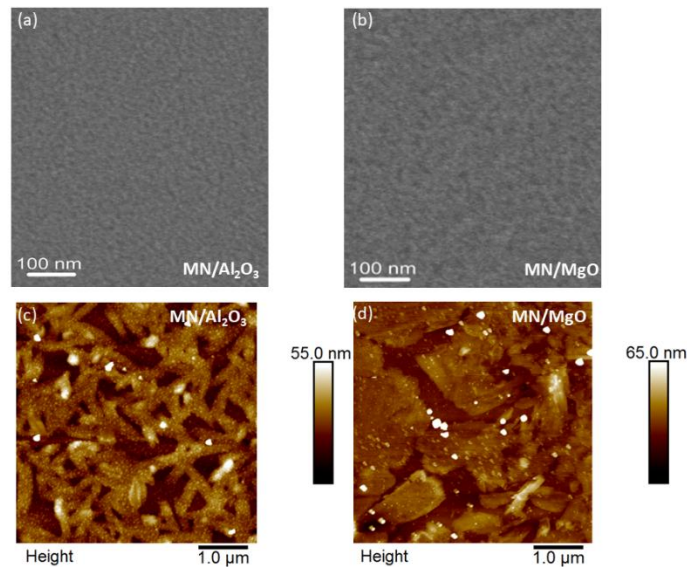


Figure S2. SEM images of (a) MN/Al₂O₃ and (b) MN/MgO. AFM images of (c) MN/Al₂O₃ and (d) MN/MgO.

(B) SEM and AFM analysis:

Figure S2 (a-b) shows SEM images of films, where MN/Al₂O₃ has a homogeneous arrangement of grains with less volume of grain-boundaries while MN/MgO has larger grains with ridges and voids reflecting higher roughness and lower density, which is also

in line with the estimation from the XRR. The observations of higher grain boundaries in Al_2O_3 are also supported by the AFM images in Figure S2 (c-d).

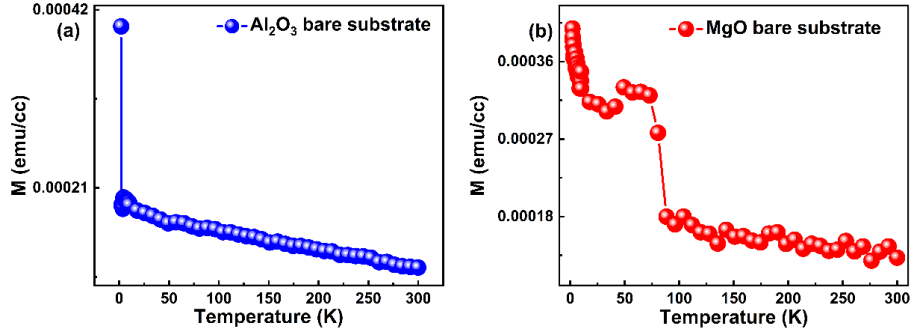


Figure S3: M-T of bare substrates (a) Al_2O_3 , (b) MgO .

(C) Magnetisation vs Temperature plots of the bare substrates.

The M–T plots (Figure S3 (a–b)) of the bare substrates exhibit no signatures of superconductivity, thereby confirming that the observed superconducting behaviour is arising from the films and not from the substrates.

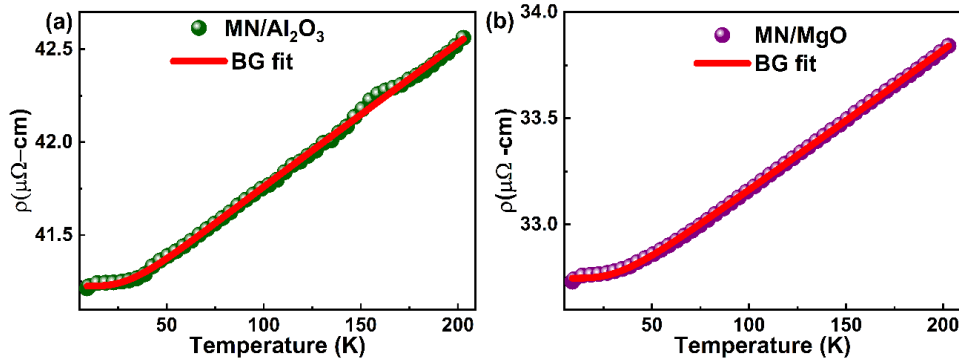


Figure S4: Bloch-Grüneisen fitting of resistivity for (a) $\text{MN}/\text{Al}_2\text{O}_3$ and (b) MN/MgO .

(D) Resistivity data analysis using Bloch-Grüneisen equation and electron phonon coupling strength estimation using McMillan's relation

The temperature dependent resistivity ($\rho(T)$) (Figure S4 (a-b)) have been fitted with the Bloch-Grüneisen (BG) model, given by $\rho(T) = \rho_0 + \alpha_{el-ph} \left(\frac{T}{\Theta_R}\right)^n \int_0^{\frac{\Theta_R}{T}} \frac{x^n}{(e^x - 1)(1 - e^{-x})} dx$, where ρ_0 corresponds to residual resistivity, Θ_R is Debye temperature, whereas α_{el-ph} , and n are material specific constants. The fitting revealed $\Theta_R \sim 194$ K for $\text{MN}/\text{Al}_2\text{O}_3$ and $\Theta_R \sim 201$ K for MN/MgO , while the exponent $n \approx 5$, which is a signature of cleaner electronic path like in

metals.[1, 2] The electron-phonon coupling strength (λ_{el-ph}) is calculated using the McMillan formula given by $\lambda_{el-ph} = \frac{-1.04 + \mu^* \ln(1.45 T_c / \Theta_R)}{((1 - 0.62 \mu^*) \ln(1.45 T_c / \Theta_R)) + 1.04}$ where μ^* is the repulsive screened Coulomb pseudopotential which is taken as 0.13, as in the case of transition metal based compounds.[3] Using the T_c and Θ_R the values of λ_{el-ph} have been estimated to be ~ 0.75 (for Mn/Al₂O₃) and ~ 0.76 (for MN/MgO). These results support the observations of in-plane compressive strain in Mn/MgO enhances the electron-phonon interactions compared to the tensile strain in Mn/Al₂O₃.

References:

1. J. M. Ziman, *Electrons and phonons: the theory of transport phenomena in solids*. 2001: Oxford university press.
2. A. Bid, A. Bora, and A. K. Raychaudhuri, *Temperature dependence of the resistance of metallic nanowires of diameter ≥ 15 nm: Applicability of Bloch-Grüneisen theorem*. Physical Review B, 2006. **74**(3): p. 035426.
3. W. L. McMillan, *Transition Temperature of Strong-Coupled Superconductors*. Physical Review, 1968. **167**(2): p. 331-344.